RESEARCH ARTICLE

Check for updates

NiMoO$_4$ nanorod deposited carbon sponges with ant-nest-like interior channels for high-performance pseudocapacitors†

Yunpeng Huang, [a] Fen Cui, [b] Yan Zhao, [a] Jiabiao Lian, [a] Jian Bao, [a] Tianxi Liu *[c] and Huaming Li *[a,b]

The mounting challenges of global energy shortage and climate change call for the development of low-cost and high performance energy storage systems. Here, we propose the facile preparation of a 3D sponge electrode material by the uniform deposition of NiMoO$_4$ nanorods on a carbonized melamine sponge (CMS) during a solvothermal reaction. Under the templating of a macroporous CMS backbone, the obtained 3D hierarchical NiMoO$_4$/CMS composite sponge can offer numerous electrochemical sites for faradaic redox reactions and also provide interconnected conducting carbon networks for direct and rapid charge transfer. Particularly, the unique ant-nest-like interior channels in the NiMoO$_4$/CMS composite sponge can ensure fast ion transportation and also buffer the volume change of NiMoO$_4$ during the long-term cycling. Benefiting from these advantages, the NiMoO$_4$/CMS composite electrode exhibits a high specific capacitance of 1689 F g^{-1} at 1 A g^{-1}, which outperforms most of the previously reported NiMoO$_4$-based electrodes. Moreover, the asymmetric supercapacitor device fabricated utilizing the composite sponge as a binder-free positive electrode also delivers a superior cycling stability (91.9% capacity retention after 2500 cycles) and a high energy density of 48.8 W h kg^{-1} at a power density of 800 W kg^{-1}. Hence, the current study provides a new protocol for the low-cost fabrication of 3D sponge-like electrodes towards practical supercapacitor applications.

1. Introduction

In recent years, high-performance and environmentally friendly energy-storage systems, such as fuel cells, lithium-ion batteries, and supercapacitors, have attracted considerable research attention in view of the ever growing energy and environmental challenges.[1–6] Among all the presently existing electrochemical energy-storage systems, supercapacitors have received the most intensive interest due to their higher power density (more than 10 kW kg^{-1}), higher charge/discharge rate (within seconds) and longer cycle life (more than 10^5 cycles).[7–13] Based on the energy storage mechanism, supercapacitors can be rationally divided into electric double layer capacitors (EDLCs) and pseudocapacitors (PCs); EDLCs deliver double-layer capacitance through the electrostatic storage of charges, while PCs generate high pseudocapacitance utilizing fast and reversible redox reactions on the surface. Generally, PCs containing conducting polymers or transition metal oxides can deliver capacitance 10 times higher than EDLCs. Hence, many previous research studies were focused on pseudocapacitive or redox-active electrode materials.[14–19]

Recently, binary metal oxides have been considered as promising PC electrode materials regarding their rich redox reactions and higher electrical conductivity with respect to single metal oxides.[20–23] Particularly, metal molybdate compounds MMoO$_4$ (M = Co, Zn, Ni, Mn, Fe, *etc.*) have recently emerged as potential advanced electrode materials for PCs because of their unique electrochemical properties.[24–28] In particular, NiMoO$_4$ is anticipated to be a desirable electrode material due to its high electrochemical activity of Ni and high electrical conductivity of Mo.[29,30] Nonetheless, NiMoO$_4$ still suffered from limited conductivity and poor electrochemical stability originating from the structural collapse during long-cycle redox reactions, thus leading to the drastic capacitance reduction of the NiMoO$_4$ electrode. In addition, due to the short diffusion distance (about 20 nm) of electrolytes into the

[a]*Institute for Energy Research, Jiangsu University, Zhenjiang, 212013, PR China. E-mail: lhm@ujs.edu.cn*
[b]*School of Chemistry and Chemical Engineering, Jiangsu University, Zhenjiang, 212013, PR China*
[c]*State Key Laboratory for Modification of Chemical Fibers and Polymer Materials, College of Materials Science and Engineering, Donghua University, Shanghai 201620, China. E-mail: txliu@dhu.edu.cn*
†Electronic supplementary information (ESI) available. See DOI: 10.1039/c8qi00247a

1594 | *Inorg. Chem. Front.*, 2018, **5**, 1594–1601

This journal is © the Partner Organisations 2018

pseudocapacitive electrodes,[31] only the superficial layer of the electrode materials can be involved in the redox reactions and the majority of the active materials are isolated from the electrolyte, resulting in a very limited efficiency of the active materials. Therefore, to increase the efficiency and electrochemical stability of electrode materials, rational construction of the $NiMoO_4$ electrode with favorable micro/nanostructures is very urgent.

Two effective strategies are proposed to deal with the aforementioned issues. One effective strategy to increase the intrinsic low electrical conductivity of metal oxides is to directly grow active materials on conductive substrates. Second, *via* the rational construction of hierarchical nanostructures, such as 1D nanoneedles/nanowires or 2D nanosheets, the internal resistance to electron transport can be relieved and the ion diffusion pathways can be shortened, which is helpful in increasing the accessible electro-active sites and improving the utilization efficiency of the electrode materials. Combining both strategies, it is believed that significant enhancement in capacitive performance can be realized if the carefully designed $NiMoO_4$ hierarchical nanostructures are well hybridized with the conducting substrates. For example, Wang and coworkers[26] deposited $NiMoO_4$ nanowires on conductive carbon cloth, obtaining a specific capacitance of 1587 F g^{-1} at 5 mA cm^{-2}. Kumar Das and coworkers[25] hybridized $NiMoO_4$ nanorods with graphene through a hydrothermal procedure, and the obtained electrode delivered a capacitance of 367 F g^{-1} at 5 A g^{-1} and an energy density of 10.32 W h kg^{-1} at a power density of 1125 W kg^{-1}. Lou *et al.*[32] proposed the controllable synthesis of $NiMoO_4$ nanosheets and nanorods on various conductive substrates for pseudocapacitors, which also showed an improved capacitance of 1221.2 F g^{-1} at 1 A g^{-1}. On the other side, with the quick development of portable and wearable electronic devices, flexible power sources are becoming increasingly important for the modern electronic industries.[33–35] In this circumstance, flexible and robust electrode materials are a prerequisite to fabricate flexible energy devices.

Porous three-dimensional (3D) electrodes, such as 3D graphene aerogels/foams,[36,37] 3D CNT aerogels,[38] nickel foam,[39] stainless steel mesh,[40] and carbonaceous 3D foams,[41] have attracted much attention due to their 3D interconnected networks and multi-dimensional porosity, thus affording fast charge and mass transfer through numerous electron/ion pathways during an electrochemical process. Commercial low-cost polymer foams/sponges, such as melamine sponges (MS), can be facilely carbonized into light-weight and flexible carbon sponges, which can be used as ideal substrates for the large-scale production of free-standing/flexible electrode materials.

Herein, we focus on the rational design of the $NiMoO_4$ nanorod deposited composite carbon sponge as a free-standing and compressive 3D electrode for high-performance supercapacitors. The carbonized melamine sponge (CMS) with 3D interconnected networks and macro-pores is first prepared through high temperature carbonization, and the $NiMoO_4$ nanorods are then successfully grown on CMS frameworks by a template-assisted solvothermal reaction. The 3D macroporous skeleton not only directs the uniform growth of the

$NiMoO_4$ nanorods, thus greatly increasing the electrochemically active sites, but the interconnected carbon networks also serve as a conducting backbone to promote the charge transfer. More importantly, the ant-nest-like interior channels inside the composite sponge also serve as fast channels for electrolyte diffusion. Benefiting from these unique advantages, the as-synthesized 3D $NiMoO_4$/CMS composite sponge manifests superior electrochemical performance as a supercapacitor electrode (specific capacitance of 1689 F g^{-1} at 1 A g^{-1}); the assembled asymmetric supercapacitor device also delivers both high energy density of 48.8 W h kg^{-1} at a power density of 800 W kg^{-1} and manifests excellent long cycling stability with a capacitance retention of 91.9% after 2500 cycles.

2. Experimental

2.1 Materials

The melamine sponge (MS) used in the experiments was obtained from SINOYQX (Sichuan, China). $Na_2MoO_4 \cdot 7H_2O$ (99.99%) and $Ni(NO_3)_2 \cdot 6H_2O$ (99.99%) were purchased from Sinopharm Chemical Reagent Co. Ltd. *N,N*-dimethylformamide (DMF) and ethanol were obtained from Shanghai Chemical Reagent Company.

2.2 Synthesis of the $NiMoO_4$/CMS composite sponge

The procedure for the synthesis of the 3D $NiMoO_4$/CMS composite sponge is schematically presented in Scheme 1. In a typical experiment, MS was carefully tailored into thin strips with a size of about 50 × 15 × 2 mm^3, after thoroughly rinsing with ethanol and acetone under ultrasonication for 30 min, and the dried MS strips were carbonized in a tubular furnace under an N_2 atmosphere at a heating rate of 10 °C min^{-1} up to 800 °C and held for 2 h. After cooling to room temperature, the obtained CMS was immersed in HNO_3 solution for 1 h to remove any impurities, and then washed with DI water several times. To grow $NiMoO_4$ onto the CMS, the reaction solution was first prepared by dissolving 20 mmol $Na_2MoO_4 \cdot 7H_2O$ and 20 mmol $Ni(NO_3)_2 \cdot 6H_2O$ in DI water. Then, 2 mg 1 × 2 cm^{-2} pre-treated CMS was immersed in the above mixed solution
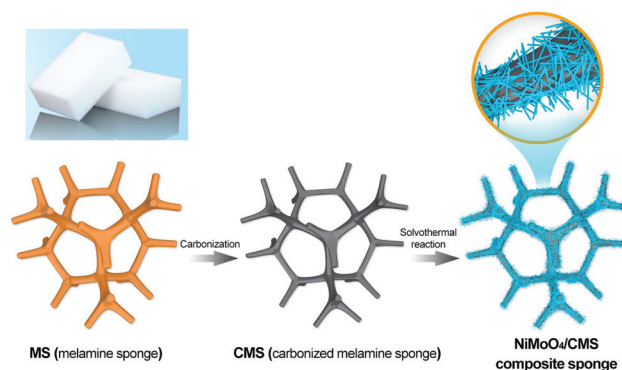
Scheme 1 Schematic for the preparation of the $NiMoO_4$/CMS composite sponge.

and transferred to a 40 mL Teflon-lined stainless steel auto-clave. After 6 h of solvothermal reaction at 160 °C, the CMS covered with the light green $NiMoO_4$ hydrate precursor was taken out and washed several times with DI water to remove any unattached products. Finally, the $NiMoO_4$/CMS composite sponge was obtained through the annealing treatment of the precursor deposited sponge at 400 °C for 60 min under an N_2 atmosphere. Pure $NiMoO_4$ was also synthesized under the same conditions in the absence of any substrates.

2.3 Material characterization

The microstructural properties of all samples were characterized using SEM (JEOL JSM-7001F) and TEM (Tecnai G2 20 TWIN TEM). The crystal structure of the products was studied using X-ray diffraction (XRD) on a Bruker D8 diffractometer in the 2θ range of 10–80° at room temperature (Cu Kα radiation, λ = 1.5418 Å). X-ray photoelectron spectroscopy (XPS) was carried out on a Kratos AXIS Ultra DLD. The specific surface area and pore size distribution were characterized with a Belsorp-max surface area detecting instrument (Tristar 3000) by N_2 physisorption at 77 K.

2.4 Electrochemical measurements

The electrochemical measurements were studied using a Gamry Interface 5000P electrochemical workstation (Gamry Instruments, America) in a three-electrode system in aqueous 3 M KOH solution. The self-standing $NiMoO_4$/CMS composite sponge was directly used as the working electrode without using any binder or conducting additives. A Pt electrode and an Hg/HgO were used as the counter electrode and the reference electrode, respectively. The immersed area of the electrodes was kept at about $1cm^2$, and the average mass loading of $NiMoO_4$ on the CMS was determined to be 1.6 mg cm^{-2} by careful weighing after annealing. Cyclic voltammetry (CV) was performed between 0 and 0.5 V; electrochemical impedance spectroscopy (EIS) was carried out from 10^{-2} to 10^6 Hz with an amplitude of 5 mV. The specific capacitance (C_s) was calculated from the discharge curves, according to the following eqn (1):

$$C_s = I\Delta t/m\Delta V \qquad (1)$$

where I is the constant discharge current, Δt is the discharge time, m is the active mass loading of the working electrode, and ΔV is the discharge voltage.

2.5 Supercapacitor devices

The asymmetric supercapacitor device was assembled using the $NiMoO_4$/CMS composite sponge as the positive electrode and the activated carbon (AC) as the negative electrode. The AC electrode was prepared by mixing 80% AC, 10% poly(vinylidene fluoride) (PVDF) powder and 10% carbon black in N-methylpyrrolidinone (NMP) to form a homogeneous slurry, followed by pressing onto nickel foam and drying. A 3 M KOH solution was utilized as the electrolyte and a commercial cellulose fibrous membrane was used as the separator (the device was denoted as CMS/NMO//AC ASCs). The energy density (E)

and power density (P) of the device were calculated according to the following equations:

$$E = C\Delta V^2/2 \qquad (2)$$

$$P = E/\Delta t \qquad (3)$$

where C is the specific capacitance, ΔV is the discharge voltage, and Δt is the discharge time.

3. Results and discussion

3.1 Morphology and structure

MS was used in this work to prepare a 3D carbon sponge, which is mainly composed of formaldehyde–melamine resin, and is usually utilized as an abrasive cleaner and soundproofing material. As presented in Fig. 1A, the commercially available MS shows a well-defined 3D interconnected configuration with a concave triangular fiber shape. The CMS can be easily obtained through a direct carbonization of MS at 800 °C for 2 h under an inert atmosphere, where a great volume shrinkage occurs after the high-temperature treatment (Fig. S1†). In spite of the shape change, the CMS almost retains the 3D networks of MS. As demonstrated in Fig. 1B, the interconnected 3D CMS framework is composed of abundant cellular structures with pore diameters of about 50–70 μm., which also shows extremely low density (about 5 mg cm^{-3}) and high porosity (about 99.6%). Additionally, the CMS demonstrates pretty good flexibility and resilience, which can withstand a large scale bend and twist deformation (Fig. S2A and B†). The structural stability of the CMS may be attributed to its interconnected 3D carbon networks, which can endure stress and load from all directions. The excellent structural properties make CMS a perfect substrate for constructing 3D flexible electrodes.

$NiMoO_4$ was subsequently grown on a CMS sponge by a simple hydrothermal reaction coupled with an annealing treatment. To optimize the growth of $NiMoO_4$, the concentrations of $Na_2MoO_4\cdot7H_2O$ and $Ni(NO_3)_2\cdot6H_2O$ were adjusted to 10 mmol, 20 mmol, 30 mmol and 40 mmol, with the resulting products denoted as $NiMoO_4$/CMS-10, $NiMoO_4$/CMS-20, $NiMoO_4$/CMS-30 and $NiMoO_4$/CMS-40, respectively. At low concentrations, many small particles can be found scattered on the surface of the CMS (Fig. S3A†), and the majority of the CMS surface is left exposed. On increasing the precursor concentration to 20 mmol, substantial rod-like $NiMoO_4$ nano-
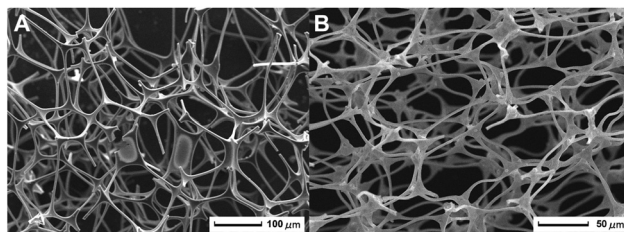

Fig. 1 SEM images of (A) MS and (B) CMS.

1596 | *Inorg. Chem. Front.*, 2018, **5**, 1594–1601

This journal is © the Partner Organisations 2018

structures are obtained and uniformly deposited on the CMS sponge to form a well-defined ant-nest-like hierarchical architecture (Fig. 2A and the inset), where no aggregates can be observed and the inter-connected interior channels of the CMS sponge are largely maintained to facilitate efficient electrolyte transportation (Fig. 2B). Moreover, the NiMoO$_4$ nanorods with the length of 6–10 μm are grown on the CMS skeleton in a prone position, and intersect with each other in a random orientation (Fig. 2C and D). It is also notable that there exist a few sphere-like particles among the nanorods, which may be ascribed to the different morphology of NiMoO$_4$ (Fig. 2C). Elemental mapping and elemental distribution shown in Fig. 2E and S4† identify the well-defined distribution of the corresponding element of C, Ni, Mo, and O in the NiMoO$_4$/CMS-20 composite sponge.

On further increasing the concentration from 30 mmol to 40 mmol, self-aggregates of the NiMoO$_4$ nanorods and severe collapse of the macro-porous architecture start to appear on NiMoO$_4$/CMS-30 and NiMoO$_4$/CMS-40 (Fig. S3B and S3C†), and most of the macro-pores and channels are blocked by the overgrown NiMoO$_4$ nanorods. These morphological characterization tentatively indicates the controllable synthesis of the 3D NiMoO$_4$/CMS composite sponge. The morphology of pure NiMoO$_4$ was also observed by SEM (Fig. S3D†), which exhibits an aggregated spherical structure, indicating that the CMS can serve as a good substrate for the uniform growth of NiMoO$_4$. Meanwhile, the digital image in Fig. S5† indicates that the composite sponge perfectly inherits the structural stability of the CMS, and no crack and shrinkage can be observed on the NiMoO$_4$/CMS-20 composite sponge. A bending test also reveals that the flexibility and robustness of the composite sponge is
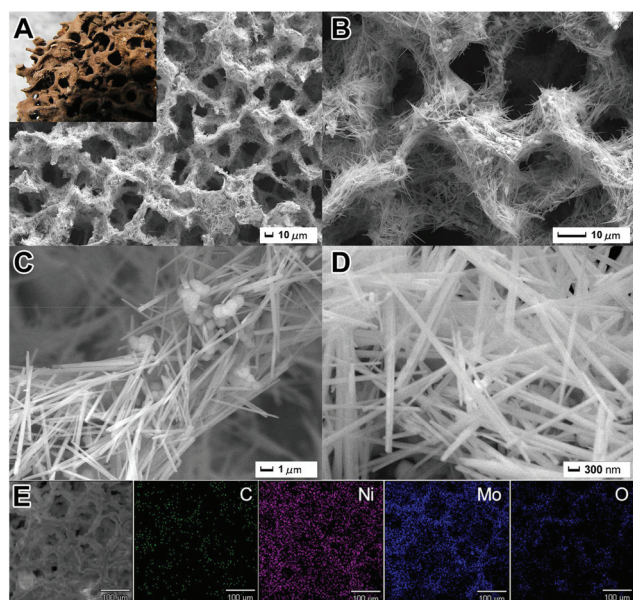
largely maintained, which is favorable for the practical applications in flexible supercapacitors. The Brunauer–Emmett–Teller (BET) analyses show that the NiMoO$_4$/CMS-20 composite sponge has a high specific surface area of 39.8 m^2 g^{-1} (Fig. S6†), and the distribution of the nano-sized pores in the inset of Fig. S6† may be attributed to the micropores between the NiMoO$_4$ nanorods.

Fig. 3A shows the typical TEM image of the NiMoO$_4$ nanorods on the NiMoO$_4$/CMS-20 composite sponge, which presents a uniform rod-like nanostructure with a diameter of about 100 nm. In addition, the HRTEM image in Fig. 3B reveals the well-defined lattice fringes with an interplanar spacing of 0.27 nm, corresponding to the (222) planes of the NiMoO$_4$ nanorods. The crystal structures of the prepared NiMoO$_4$/CMS-20 composite sponge were studied using XRD as shown in Fig. 4. The pattern of the CMS substrate exhibits a diffraction peak at about 25°, corresponding to the (002) peak of amorphous carbon. The diffraction peaks of the NiMoO$_4$/CMS-20 composite sponge at around 14.5°, 27.1°, 29.1°, 33°, 38.3° and 44.6° can be readily indexed to the (110), (112), (220), (222), (003) and (330) crystal planes of NiMoO$_4$ (JCPDS card no. 86-0361), respectively. No signals of impurities, e.g. precursors, nickel or molybdenum oxides, have been detected, demonstrating the synthesis of pure NiMoO$_4$.

To further investigate the chemical composition of the synthesized NiMoO$_4$/CMS-20 composite sponge, XPS analysis was performed with the results shown in Fig. 5. A survey spectrum indicates the individual peaks of the Ni, O, Mo, and C elements, and no other impurity peaks can be detected (Fig. 5A). The C element may be attributed to the inevitable
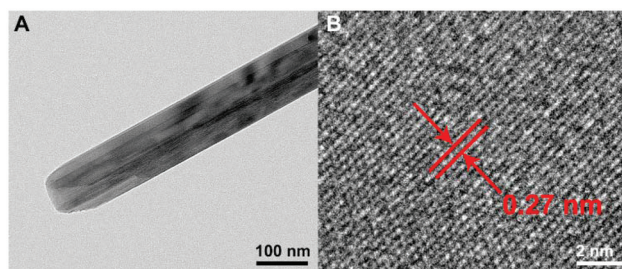

Fig. 2 SEM images of the NiMoO$_4$/CMS-20 composite sponge at (A, B) low and (C, D) high magnifications; (E) elemental mapping of NiMoO$_4$/CMS-20. The inset of (A) is a digital photograph which shows the typical configuration of a moisture ants' nest.[42]

Fig. 3 TEM images of NiMoO$_4$ nanorods in the NiMoO$_4$/CMS-20 composite sponge at low (A) and high (B) magnifications.
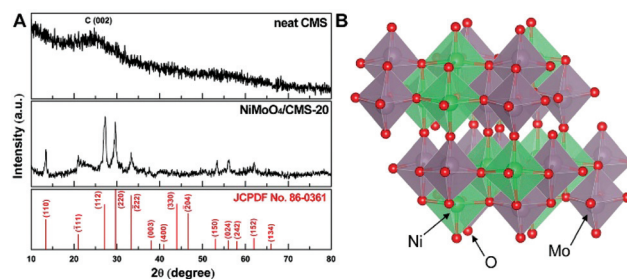
Fig. 4 (A) XRD patterns of neat CMS and NiMoO$_4$/CMS-20; (B) crystal structure of NiMoO$_4$.

This journal is © the Partner Organisations 2018

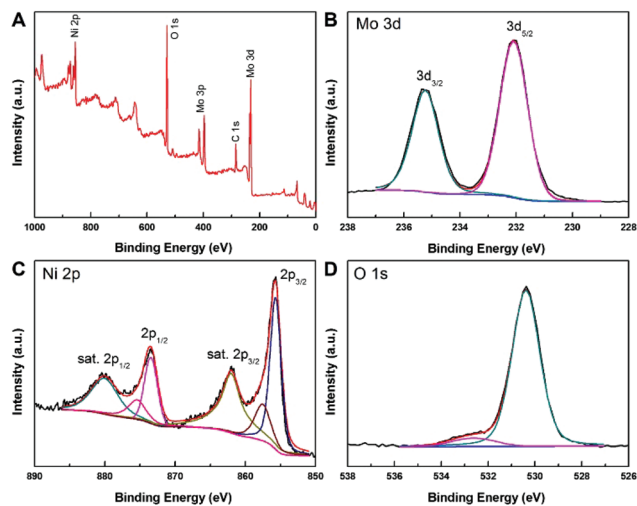*Inorg. Chem. Front.*, 2018, **5**, 1594–1601 | **1597**

Fig. 5 XPS spectra of NiMoO$_4$/CMS-20: (A) survey spectrum and the core-level spectra of (B) Mo 3d, (C) Ni 2p and (D) O 1s.

contamination of organic matter. The high-resolution Mo 3d spectrum reveals two major peaks of Mo 3d$_{3/2}$ and Mo 3d$_{5/2}$ at 235 eV and 232 eV (Fig. 5B), which are separated by a binding energy of 3 eV, indicating the chemical state of Mo^{6+}.[43] The Ni 2p spectrum in Fig. 5C can be reasonably deconvoluted into four peaks. The peak at 855.2 eV and its satellite peak located at 861.5 eV can be attributed to Ni 2p$_{3/2}$, whereas, the peak at 873 eV and its satellite peak at 879.6 eV correspond to the Ni 2p$_{1/2}$ level. The binding energy gap between the Ni 2p$_{3/2}$ peak and the Ni 2p$_{1/2}$ peak is 17.8 eV, suggesting the +2 oxidation state of Ni.[44] For the spectrum in Fig. 5D, the peak at 530.2 eV can be assigned to the O 1s level in NiMoO$_4$,[30] and the weak peak located at 532.7 eV can be attributed to the physically or chemically absorbed H$_2$O on the surface.[45,46] Moreover, the detailed elemental analysis indicates that the surface atomic ratio of Ni/Mo/O is 1 : 1.1 : 3.9, which is close to the formula of NiMoO$_4$. The above XPS results further confirm the successful preparation of the NiMoO$_4$/CMS composite sponge.

3.2 Electrochemical performance of NiMoO$_4$/CMS electrodes

Three-electrode cells were used to evaluate the electrochemical performance of the NiMoO$_4$/CMS composite sponges, pure NiMoO$_4$ and neat CMS. As shown in Fig. 6A, the neat CMS sponge exhibits noticeable electric double-layer capacitive performance; meanwhile, the CV curves of the NiMoO$_4$/CMS composite sponges show the distinguishable pseudocapacitive nature of transition metal oxides. Well-defined redox peaks can be clearly observed in the potential window of 0.1 to 0.5 V vs. SCE for all three composite electrodes, which can be attributed to the faradaic redox reactions related to Ni^{2+} ↔ Ni^{3+} + e$^-$. Compared with the pure NiMoO$_4$ and neat CMS electrodes, the NiMoO$_4$/CMS composite electrodes manifest much higher capacitive performance due to the deposition of electrochemically active NiMoO$_4$ nanorods and fast charge transfer paths provided by the 3D CMS backbone. Remarkably, among the
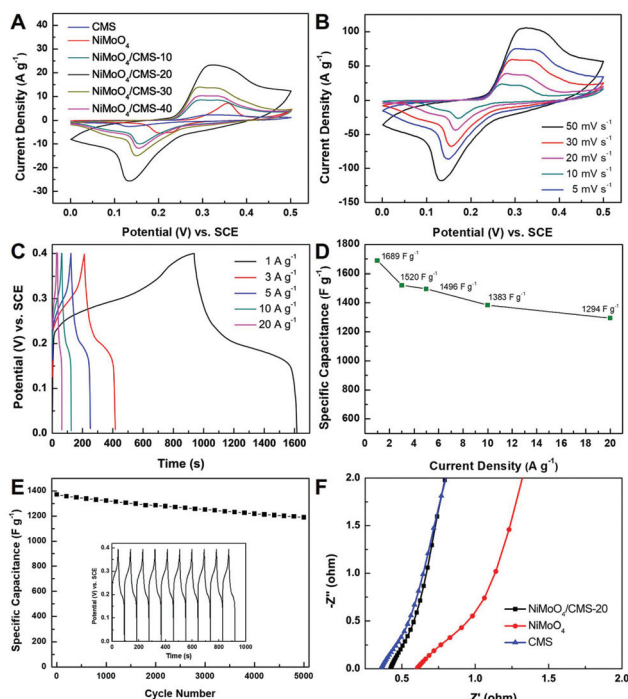

Fig. 6 (A) CV curves of neat CMS, pure NiMoO$_4$, and NiMoO$_4$/CMS composites at a scan rate of 5 mV s^{-1}; (B) CV curves of the NiMoO$_4$/CMS-20 composite electrode at various scan rates; (C) galvanostatic charge–discharge curves of the NiMoO$_4$/CMS-20 electrode at various current densities; (D) specific capacitance of the NiMoO$_4$/CMS-20 electrode at various current densities; (E) the long-term cycling performance of the NiMoO$_4$/CMS-20 electrode at a current density of 10 A g^{-1}; (F) Nyquist plots of NiMoO$_4$/CMS-20, pure NiMoO$_4$, and neat CMS electrodes.

NiMoO$_4$/CMS composite electrodes, the current density and the area of the CV curve of the NiMoO$_4$/CMS-20 electrode are obviously larger than those of the NiMoO$_4$/CMS-10, NiMoO$_4$/CMS-30 and NiMoO$_4$/CMS-40 electrodes, indicating the superior electrochemical performance of the NiMoO$_4$/CMS-20 composite sponge, which can be attributed to the most uniform distribution of the NiMoO$_4$ nanorods and well maintained ant-nest-like interior channels of NiMoO$_4$/CMS-20. Fig. 6B displays the CV curves of the NiMoO$_4$/CMS-20 electrode at various scan rates from 5 to 50 mV s^{-1}, within the potential range from 0.1 to 0.5 V vs. SCE, the peak current increases almost linearly with the scan rate, implying the rapid transportation of electrons and ions during the faradaic process. In addition, the redox peaks slightly shifted along with the increment of the scan rate, indicating that the NiMoO$_4$/CMS-20 electrode favors the fast redox reaction.

To further evaluate the electrochemical performance of the NiMoO$_4$/CMS-20 composite sponge, galvanostatic charge–discharge measurements were conducted in the potential range of 0–0.4 V vs. SCE at various current densities. As presented in Fig. 6C, the charge–discharge curves show a distinct plateau region at current densities from 1 to 20 A g^{-1}, further revealing the pseudocapacitive characteristics of the electrode. Based on the discharge time, the specific capacitance of the NiMoO$_4$/

CMS-20 electrode can be calculated (using eqn (1)) to be 1689 F g^{-1} at a current density of 1 A g^{-1} (based on the active materials), which outperforms those previously reported NiMoO$_4$-based electrodes (Table S1†). Furthermore, it is remarkable to note that 76.6% of the capacitance (1294 F g^{-1}) is still retained even at a high current density of 20 A g^{-1} (Fig. 6D), which is ascribed to the fast charge transfer and electrolyte diffusion through the networked CMS backbone and interconnected ant-nest-like channels. As a critical requirement for practical applications, the long-term cycling stability of the electrode was also evaluated. As shown in Fig. 6E, 86.7% of the specific capacitance can be maintained after 5000 charge/discharge cycles at a current density of 10 A g^{-1}, indicating the excellent long-term electrochemical stability of the NiMoO$_4$/CMS-20 composite sponge. The first ten charge/discharge curves of the electrode are shown in the inset of Fig. 6E. Fig. 6F compares the Nyquist plots of the NiMoO$_4$/CMS-20, NiMoO$_4$, and CMS electrodes at an open-circuit potential. The absence of a semicircle in the high-frequency region for all the electrodes may be caused by the high charge transfer process. It is obvious that the series resistance (R_s, x-intercept of Nyquist plots) of the NiMoO$_4$/CMS-20 electrode is close to that of the CMS and is much lower than that of the pure NiMoO$_4$ electrode, indicating that the conducting CMS networks can largely increase the charge transfer speed of the NiMoO$_4$/CMS-20 composite sponge, further highlighting the rational design of this 3D hierarchical composite sponge. Furthermore, the more vertical slopes of the NiMoO$_4$/CMS-20 electrode in the low-frequency region also demonstrate the low ion diffusion and charge transfer resistance.

The enhanced electrochemical performance of the NiMoO$_4$/CMS-20 composite sponge can be attributed to the following three features of this unique 3D hierarchical structure (Scheme 2). First, the 3D networks of the CMS with abundant macro-pores can realize the uniform deposition of the NiMoO$_4$ nanorods, thus largely increasing the available electrochemically active sites for efficient faradaic redox reactions. Second, due to the intimate contact between the CMS skeleton and NiMoO$_4$ nanorods, the generated electrons during the redox reactions can be transferred directly and rapidly through the conducting CMS networks. Third, the formed ant-nest-like interior channels in the NiMoO$_4$/CMS-20 composite sponge can ensure fast electrolyte transportation, and also buffer the volume expansion/shrinkage of NiMoO$_4$ during the long-term charge/discharge process, hence resulting in a high specific capacitance and excellent cycling stability. Therefore, the synergetic contribution of the CMS backbone and NiMoO$_4$ nanorods in the 3D hierarchical architecture makes the NiMoO$_4$/CMS composite sponge a remarkable supercapacitor electrode material.

3.3 Capacitive performance of asymmetric supercapacitors

To find out the potential of the prepared NiMoO$_4$/CMS composite sponge for practical applications, an asymmetric supercapacitor device was fabricated using the NiMoO$_4$/CMS composite sponge as the anode and the AC electrode as the cathode
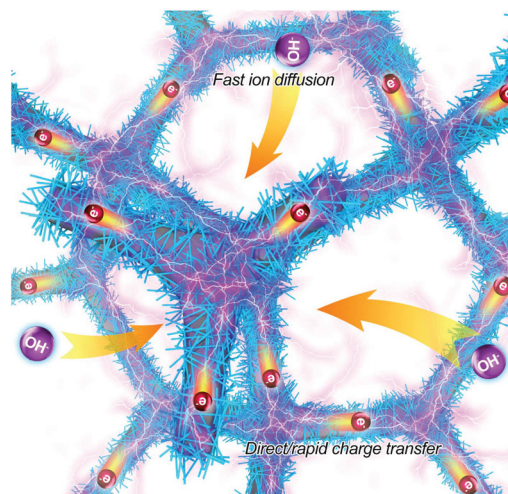
Scheme 2 Schematic illustration showing the fast ion diffusion and direct charge transfer during the faradaic redox reaction on the NiMoO$_4$/CMS composite electrode.

(Fig. 7A). The AC electrode exhibits significant electric double-layer capacitive characteristics in terms of near-rectangular CV curves (Fig. S76A†), along with symmetrical and linear charge/discharge curves (Fig. S7B†). The specific capacitance of the AC electrode is calculated to be 142.5 F g^{-1} at 0.5 A g^{-1} accord-
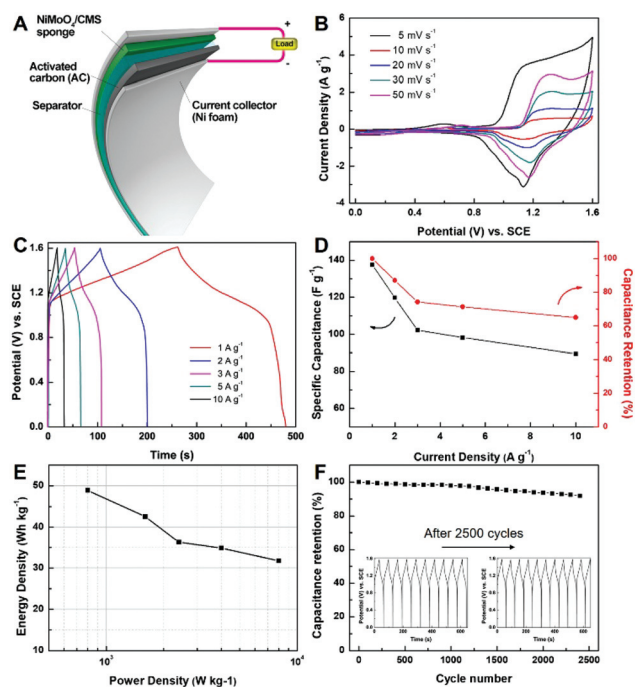

Fig. 7 (A) Schematic of the structure of the CMS/NMO//AC ASC device; (B) CV curves of the device at various scan rates; (C) galvanostatic charge–discharge curves of the supercapacitor at various current densities; (D) specific capacitance and the corresponding capacitance retention of the assembled ASC device at different current densities; (E) Ragone plots of the device; (F) long-term cycling stability of the supercapacitor at a current density of 5 A g^{-1}.

This journal is © the Partner Organisations 2018

Inorg. Chem. Front., 2018, **5**, 1594–1601 | **1599**

ing to its charge/discharge curves (Fig. S7C†). To find out the best mass combination between the anode and the cathode, four asymmetric supercapacitor devices were fabricated with different AC mass loadings, i.e., 4 mg, 8 mg, 16 mg, and 20 mg. As shown in Fig. S8,† when the mass of the AC electrodes is below 16 mg, a distinct increase in the CV current can be observed. However, on further raising the AC mass to 20 mg, the capacitance of the device decreases due to the less contribution of AC per square meter, indicating that the charges do not balance under this circumstance. Therefore, 16 mg of AC is appropriate for the asymmetric supercapacitor device.

The fabricated CMS/NMO//AC ASCs manifest excellent capacitive performance at the potential range of 0–1.6 V under the collaborative contribution of electric double-layer capacitance and pseudocapacitance (Fig. 7B). The configuration of the CV curves is well kept even at a high scan rate of 50 mV s^{-1}, demonstrating the fast charge–discharge kinetics of the ASCs. Galvanostatic charge/discharge measurements were performed to further study the electrochemical performance of the CMS/NMO//AC ASCs. The plateau region in the curves is attributed to the faradaic redox reaction of the anode (Fig. 7C). In addition, the specific capacitance of the device based on the total mass is calculated to be 137.5, 119.6, 102.2, 98.1, and 89.4 F g^{-1} at current densities of 1, 2, 3, 5, and 10 A g^{-1} respectively (Fig. 7D). Notably, the CMS/NMO//AC ASC device manifests good rate capability with 65% of capacitance retention at a high current density of 10 A g^{-1}. Energy density (E) and power density (P) are the two important factors for the practical applications of supercapacitors. Based on eqn (2) and (3), the energy density and power density of the CMS/NMO//AC ASC device are calculated and plotted on the Ragone plots. As presented in Fig. 7E, the device shows the maximum energy density of 48.8 W h kg^{-1} at a power density of 800 W kg^{-1}, and an energy density of 31.8 W h kg^{-1} at a high power density of 8000 W kg^{-1}. These results are superior to many previously reported values such as CBC-N@LDH (36.3 W h kg^{-1} at 800.2 W kg^{-1}),[47] Co$_3$O$_4$@NiMoO$_4$ nanosheet arrays (37.8 W h kg^{-1} at 482 W kg^{-1}),[48] and NiCo$_2$O$_4$@NiMoO$_4$ core–shell NWSAs on Ni foam (21.7 W h kg^{-1} at 157 W kg^{-1}).[49] Furthermore, the cycling stability of the as-fabricated CMS/NMO//AC ASC device was also assessed. As presented in Fig. 7F, the device can retain a high capacitance retention of 91.9% after 2500 charge–discharge cycles, when the first and last ten charge/discharge cycles almost overlap, demonstrating the excellent durability of the CMS/NMO//AC device. After a series of electrochemical tests, an inspection of the morphology of the NiMoO$_4$/CMS-20 electrode through SEM and elemental mapping (Fig. S9A–C†) reveals that the composite sponge can well maintain its hierarchical structures, further confirming the structural stability of the NiMoO$_4$/CMS-20 composite sponge.

4. Conclusions

In summary, we have introduced the NiMoO$_4$ nanorod deposited macroporous carbon sponge with ant-nest-like interior channels through a template-assisted solvothermal reaction, which exhibits excellent capacitive performance as an asymmetric supercapacitor electrode. The electrically conductive CMS skeleton with abundant macro-pores not only mediates the uniform deposition of the NiMoO$_4$ nanorods to expose more electrochemically active sites, but also realizes the direct and rapid charge transfer through the conducting CMS networks. Specially, the ant-nest-like interior channels in the NiMoO$_4$/CMS composite sponge can ensure fast electrolyte transportation, and also buffer the drastic volume change of NiMoO$_4$ during the long-term cycling. These characteristics synergistically lead to the superior electrochemical performance of the NiMoO$_4$/CMS composite sponge in terms of high specific capacitance (1689 F g^{-1} at 1 A g^{-1}), and excellent cycling stability (86.7% after 5000 cycles at a current density of 10 A g^{-1}). Additionally, the assembled asymmetric supercapacitor device fabricated using the composite sponge as a binder-free electrode also delivers a superior cycling stability (91.9% capacity retention after 2500 cycles), and a high energy density of 48.4 W h kg^{-1} at a power density of 800 W kg^{-1}, further highlighting the successful design of this 3D hierarchical composite sponge for exploring high-performance next-generation energy storage devices.

Conflicts of interest

There are no conflicts to declare.

Acknowledgements

Notes and references

1 M. D. Stoller, S. Park, Y. W. Zhu, J. An and R. S. Ruoff, Nano Lett., 2008, **8**, 3498.

2 G. P. Wang, L. Zhang and J. J. Zhang, Chem. Soc. Rev., 2012, **41**, 797.

3 X. K. Huang, S. M. Cui, J. B. Chang, P. B. Hallac, C. R. Fell, Y. T. Luo, B. Metz, J. W. Jiang, P. T. Hurley and J. H. Chen, Angew. Chem., Int. Ed., 2015, **54**, 1490.

4 X. E. Liu, M. Park, M. G. Kim, S. Gupta, G. Wu and J. Cho, Angew. Chem., Int. Ed., 2015, **54**, 9654.

5 H. G. Liang, H. N. Su, B. G. Pollet and S. Pasupathi, J. Power Sources, 2015, **288**, 121.

1600 | Inorg. Chem. Front., 2018, **5**, 1594–1601

This journal is © the Partner Organisations 2018

6 H. N. Su, Q. Xu, J. J. Chong, H. M. Li, C. Sita and S. Pasupathi, *J. Power Sources*, 2017, **341**, 302.

7 C. Zhang, W. W. Tjiu and T. X. Liu, *Polym. Chem.*, 2013, **4**, 5785.

8 Y. Zhao, L. F. Hu, S. Y. Zhao and L. M. Wu, *Adv. Funct. Mater.*, 2016, **26**, 4085.

9 L. Xu, Y. Zhao, J. B. Lian, Y. G. Xu, J. Bao, J. X. Qiu, L. Xu, H. Xu, M. Q. Hua and H. M. Li, *Energy*, 2017, **123**, 296.

10 M. M. Zhang, Y. Wang, D. H. Pan, Y. Li, Z. X. Yan and J. M. Xie, *ACS Sustainable Chem. Eng.*, 2017, **5**, 5099.

11 G. X. Zhu, C. Y. Xi, Y. J. Liu, J. Zhu and X. P. Shen, *J. Mater. Chem. A*, 2015, **3**, 7591.

12 D. Tian, X. F. Lu, G. D. Nie, M. Gao and C. Wang, *Inorg. Chem. Front.*, 2018, **5**, 635.

13 D. Y. Yu, Z. Q. Zhang, Y. N. Meng, Y. F. Teng, Y. P. Wu, X. Y. Zhang, Q. S. Sun, W. M. Tong, X. D. Zhao and X. Y. Liu, *Inorg. Chem. Front.*, 2018, **5**, 597.

14 N. D. Kim, D. B. Buchholz, G. Casillas, M. José-Yacaman and R. P. H. Chang, *Adv. Funct. Mater.*, 2014, **24**, 4186.

15 Z. J. Su, C. Yang, B. H. Xie, Z. Y. Lin, Z. X. Zhang, J. P. Liu, B. H. Li, F. Y. Kang and C. P. Wong, *Energy Environ. Sci.*, 2014, **7**, 2652.

16 W. P. Si, C. L. Yan, Y. Chen, S. Oswald, L. Y. Han and O. G. Schmidt, *Energy Environ. Sci.*, 2013, **6**, 3218.

17 M. Ghidiu, M. R. Lukatskaya, M. Q. Zhao, Y. Gogotsi and M. W. Barsoum, *Nature*, 2014, **516**, 78.

18 Y. Zhang, Y. Zhao, S. S. Cao, Z. L. Yin, L. Cheng and L. M. Wu, *ACS Appl. Mater. Interfaces*, 2017, **9**, 29982.

19 Y. Zhao, L. Xu, S. Q. Huang, J. Bao, J. X. Qiu, J. B. Lian, L. Xu, Y. P. Huang, Y. G. Xu and H. M. Li, *J. Alloys Compd.*, 2017, **702**, 178.

20 S. J. Peng, L. L. Li, Y. X. Hu, M. Srinivasan, F. Y. Cheng, J. Chen and S. Ramakrishna, *ACS Nano*, 2015, **2**, 1945.

21 X. Z. Yu, B. A. Lu and Z. Xu, *Adv. Mater.*, 2014, **26**, 1044.

22 J. Zhu, Z. Xu and B. A. Lu, *Nano Energy*, 2014, **7**, 114.

23 G. Q. Zhang and X. W. Lou, *Adv. Mater.*, 2013, **25**, 976.

24 D. P. Cai, B. Liu, D. D. Wang, L. L. Wang, Y. Liu, H. Li, Y. R. Wang, Q. H. Li and T. H. Wang, *J. Mater. Chem. A*, 2014, **2**, 4954.

25 D. Ghosh, S. Giri and C. K. Das, *Nanoscale*, 2013, **5**, 10428.

26 D. Guo, Y. Z. Luo, X. Z. Yu, Q. H. Li and T. H. Wang, *Nano Energy*, 2014, **8**, 174.

27 J. H. Lin, H. Y. Liang, H. N. Jia, S. L. Chen, Y. F. Cai, J. L. Qi, J. Cao, W. D. Fei and J. C. Feng, *Inorg. Chem. Front.*, 2017, **4**, 1575.

28 J. L. Meng, J. Q. Fu, X. X. Yang, M. J. Wei, S. Liang, H. Y. Zang, H. Q. Tan, Y. H. Wang and Y. G. Li, *Inorg. Chem. Front.*, 2017, **4**, 1791.

29 W. Xiao, J. S. Chen, C. M. Li, R. Xu and X. W. Lou, *Chem. Mater.*, 2010, **22**, 746.

30 J. Haetge, I. Djerdj and T. Brezesinski, *Chem. Commun.*, 2012, **48**, 6726.

31 C. Hu, K. Chang, M. Lin and Y. Wu, *Nano Lett.*, 2006, **6**, 2690.

32 S. J. Peng, L. L. Li, H. B. Wu, S. Madhavi and X. W. D. Lou, *Adv. Energy Mater.*, 2015, **5**, 1401172.

33 X. Chen, B. Liu, C. Zhong, Z. Liu, J. Liu, L. Ma, Y. D. Deng, X. P. Han, T. P. Wu, W. B. Hu and J. Lu, *Adv. Energy Mater.*, 2017, **7**, 1700779.

34 S. Padmajan Sasikala, K. E. Lee, J. Lim, H. J. Lee, S. H. Koo, I. H. Kim, H. J. Jung and S. O. Kim, *ACS Nano*, 2017, **9**, 9424.

35 W. G. Li, X. B. Xu, C. Liu, M. C. Tekell, J. Ning, J. H. Guo, J. C. Zhang and D. L. Fan, *Adv. Funct. Mater.*, 2017, **27**, 1702738.

36 Y. Zhao, J. Liu, Y. Hu, H. H. Cheng, C. G. Hu, C. C. Jiang, L. Jiang, A. Y. Cao and L. T. Qu, *Adv. Mater.*, 2013, **25** 591.

37 L. Li, K. Wang, Z. Q. Huang, C. Zhang and T. X. Liu, *Nano Res.*, 2016, **9**, 2938.

38 H. Im, T. Kim, H. Song, J. Choi, J. S. Park, R. Ovalle-Robles, H. D. Yang, K. D. Kihm, R. H. Baughman, H. H. Lee, T. J. Kang and Y. H. Kim, *Nat. Commun.*, 2016, **7**, 10600.

39 J. Zhang, T. Wang, P. Liu, Z. Q. Liao, S. H. Liu, X. D. Zhuang, M. W. Chen, E. Zschech and X. L. Feng, *Nat. Commun.*, 2017, **8**, 15437.

40 J. H. Kim, S. T. Myung and Y. K. Sun, *Electrochim. Acta*, 2004, **49**, 219.

41 S. H. Yan, X. Zhen and G. Chao, *Adv. Mater.*, 2013, **25**, 2554.

42 C. Buell, Moisture Ants-the home inspector's little helper, http://www.buellinspections.com/moisture-ants-the-home-inspectors-little-helper/, (accessed December, 2017).

43 X. F. Xia, L. Wu, Q. L. Hao, W. J. Wang and X. Wang, *Electrochim. Acta*, 2013, **99**, 253.

44 J. Yan, Z. J. Fan, S. Wei, G. Q. Ning, W. Tong, Z. Qiang, R. F. Zhang, L. J. Zhi and W. Fei, *Adv. Funct. Mater.*, 2012, **22**, 2632.

45 V. M. Jiménez, A. Fernández, J. P. Espinós and A. R. González-Elipe, *J. Electron Spectrosc. Relat. Phenom.*, 1995, **71**, 61.

46 T. Choudhury, S. O. Saied, J. L. Sullivan and A. M. Abbot, *J. Phys. D: Appl. Phys.*, 1989, **22**, 1185.

47 F. L. Lai, Y. E. Miao, L. Z. Zuo, H. Y. Lu, Y. P. Huang and T. X. Liu, *Small*, 2016, **12**, 3235.

48 W. Hong, J. Q. Wang, P. W. Gong, J. F. Sun, L. Y. Niu, Z. G. Yang, Z. F. Wang and S. R. Yang, *J. Power Sources*, 2014, **270**, 516.

49 D. Cheng, Y. F. Yang, J. L. Xie, C. J. Fang, G. Q. Zhang and J. Xiong, *J. Mater. Chem. A*, 2015, **3**, 14348.

This journal is © the Partner Organisations 2018

Inorg. Chem. Front., 2018, **5**, 1594–1601 | **1601**